SCIENTIFIC REPORTS

OPEN

SUBJECT AREAS:
BIOPHYSICS
OPTICS AND PHOTONICS

Received
17 February 2014

Accepted
28 May 2014

Published
18 June 2014

Correspondence and requests for materials should be addressed to M.O. (malini_olivo@sbic.a-star.edu.sg)

Multifunctional Photosensitizer-Based Contrast Agents for Photoacoustic Imaging

Chris Jun Hui Ho[1], Ghayathri Balasundaram[1], Wouter Driessen[2,3], Ross McLaren[1], Chi Lok Wong[1], U. S. Dinish[1], Amalina Binte Ebrahim Attia[1], Vasilis Ntziachristos[2,4] & Malini Olivo[1,5]

[1]Singapore Bioimaging Consortium, Agency for Science, Technology and Research, Singapore, [2]Institute for Biological and Medical Imaging, Helmholtz Center Munich, Germany, [3]iThera Medical, GmbH, Germany, [4]Technical University of Munich, Germany, [5]School of Physics, National University of Ireland, Galway, Ireland.

Photoacoustic imaging is a novel hybrid imaging modality combining the high spatial resolution of optical imaging with the high penetration depth of ultrasound imaging. Here, for the first time, we evaluate the efficacy of various photosensitizers that are widely used as photodynamic therapeutic (PDT) agents as photoacoustic contrast agents. Photoacoustic imaging of photosensitizers exhibits advantages over fluorescence imaging, which is prone to photobleaching and autofluorescence interference. In this work, we examined the photoacoustic activity of 5 photosensitizers: zinc phthalocyanine, protoporphyrin IX, 2,4-bis [4-(N,N-dibenzylamino)-2,6-dihydroxyphenyl] squaraine, chlorin e6 and methylene blue in phantoms, among which zinc phthalocyanine showed the highest photoacoustic activity. Subsequently, we evaluated its tumor localization efficiency and biodistribution at multiple time points in a murine model using photoacoustic imaging. We observed that the probe localized at the tumor within 10 minutes post injection, reaching peak accumulation around 1 hour and was cleared within 24 hours, thus, demonstrating the potential of photosensitizers as photoacoustic imaging contrast agents *in vivo*. This means that the known advantages of photosensitizers such as preferential tumor uptake and PDT efficacy can be combined with photoacoustic imaging capabilities to achieve longitudinal monitoring of cancer progression and therapy *in vivo*.

Photoacoustic (PA) imaging is a rapid emerging biomedical imaging modality which provides *in vivo* functional imaging information at clinically relevant penetration depths, while maintaining high spatial resolution and image contrast, as compared to existing imaging techniques[1–3]. In PA imaging, the tissue is irradiated with a laser pulse and the light energy is absorbed by endogenous chromophores such as hemoglobin and melanin, as well as exogenous contrast agents in tissue. This causes the tissue to undergo thermoelastic expansion and generate corresponding acoustic pressure waves, which in turn can be detected via ultrasound transducer arrays. The higher penetration depth of PA imaging (5–6 cm)[1–2] over fluorescence and optical coherence tomography (OCT)[4] enables deep tissue imaging, especially in clinical settings[1].

In terms of applications, endogenous hemoglobin in blood has been used for PA imaging of the tumor vascular network in the rat brain[5], the blood-oxygenation dynamics in the mouse brain[6,7], the human arm[8], as well as breast imaging[9]. In addition, various exogenous contrast agents have been introduced to enhance the imaging contrast[10–21], such as carbon nanotubes (SWNTs)[12–14], near-infrared (NIR) dyes like indocyanine green (ICG)[15–17], as well as gold nanoparticles[18–21]. However, the clinical application of these contrast agents has been limited due to cytotoxicity issues. There have been various attempts to circumvent this problem, such as the surface modification of gold nanorods with polyethylene glycol (PEG)[22], in order to lower the cytotoxicity and increase the blood circulation time, but there still remains a need for a great leap forward towards clinical translation.

On the other hand, photodynamic therapeutic (PDT) agents, also known as photosensitizers, have been widely used in clinical trials for fluorescence imaging and PDT[23]. These photosensitizers are generally classified as porphyrins or nonporphyrins[24]. Porphyrin-based photosensitizers are further categorized as first-, second- or third- generation photosensitizers, in which protoporphyrins, chlorins and phthalocyanines fall under the second-generation category, whereas squaraines and methylene blue form part of the nonporphyrin-based photosensitizers. In this work, we examined the potential of five photosensitizers as PA contrast agents namely zinc phthalocyanine (ZnPc), protoporphyrin IX (PpIX), 2,4-bis[4-(N,N-dibenzylamino)-2,6-dihydroxyphenyl]

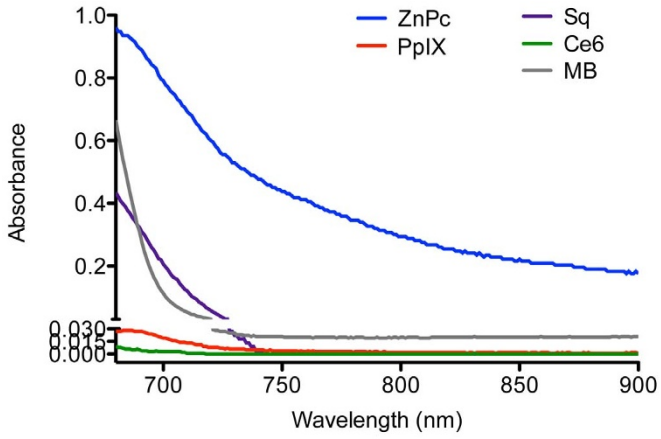

Figure 1 | Normalized absorbance as a function of wavelength for the five photosensitizers in the NIR region from 680 to 900 nm. ZnPc shows the highest overall absorbance, followed by MB, Sq, PpIX and Ce6, in decreasing order.

squaraine (Sq), chlorin e6 (Ce6) and methylene blue (MB), which, though not exhaustive, are representative of the various categories of photosensitizers, many of which have been used in clinical trials[24].To the best of our knowledge, this is the first evaluation of the various classes of photosensitizers as potential PA contrast agents. These photosensitizers exhibit low fluorescence quantum yields and thus can potentially possess high PA activity, since an excited system can either relax back to the ground state through fluorescence or thermally through internal conversion[25]. Moreover, PA imaging of photosensitizers exhibits advantages over fluorescence imaging, which is prone to photobleaching and autofluorescence interference. Because these PDT agents preferentially accumulate in tumor due to the enhanced permeation and retention (EPR) effect[26], they offer tumor-targeted PA imaging. In this paper, we first evaluated the PA performance of the five PDT agents in a scattering phantom. Next, in order to demonstrate *in vivo* PA activity and tumor-targeting efficacy, we injected ZnPc intravenously into mice and monitored the biodistribution over time using PA imaging. In light of the unique advantages such as clinical relevance, passive tumor-targeting ability and high PA activity, these photosensitizer-based PA contrast agents offer great potential in cancer diagnosis and therapy.

Results and discussion

In order to obtain information about the optical absorption properties of the contrast agents, their wavelength-dependent absorption spectra at known concentrations were measured using a spectrophotometer, which in turn were normalized to obtain the concentration-independent normalized absorbance (directly proportional to extinction coefficient) as a function of wavelength for each contrast agent (Figure 1), based on Beer-Lambert law:

$$A(\lambda) = ln\left(\frac{I_0}{I}\right) = \varepsilon(\lambda)cl$$

where $A(\lambda)$ is the measured wavelength-dependent absorbance, I_0 is the incident light intensity, I is the transmitted light intensity, $\varepsilon(\lambda)$ is the wavelength-dependent extinction coefficient of the contrast agent, c is the concentration of the contrast agent and l is the path length of the quartz cuvette (1 cm).

As shown in Figure 1, all the studied contrast agents exhibit a general decreasing trend in absorbance with increasing wavelength in the near infrared (NIR) range from 680 to 900 nm, in which ZnPc shows the highest overall absorbance, followed by MB, Sq, PpIX and Ce6 in decreasing order. Although these probes have higher reported molar extinction coefficients in the visible light range of the electromagnetic spectrum[23], and hence, are expected to provide stronger PA signals at these wavelengths, we have chosen to study the PA activity of these compounds in the NIR region from 680 to 900 nm, because at these wavelengths there is lower tissue absorption enabling imaging at greater depths. At wavelengths above 900 nm, water absorption increases significantly, making the 680–900 nm range optimal for *in vivo* deep tissue imaging.

In order to verify the PA activity of these photosensitizers under controlled conditions, we performed phantom measurements for all the contrast agents, in the 680–900 nm wavelength range, each at 5 different concentrations. The phantom is cylindrical with a diameter of 2 cm and contains 2 cylindrical channels in which contrast agents can be placed to measure the PA signal, compared to a control agent (see Figure 2A). During the data acquisition, we recorded data from multiple transverse slices across the channel portion which contains the probe and control, and applied an excitation wavelength scan from 680 to 900 nm with an interval of 10 nm for each transverse slice, and recorded the averaged PA signals from 10 frames for each wavelength and position. After image reconstruction, results showed that all the contrast agents exhibit wavelength-dependent PA activity in phantoms. In addition, there is a similar trend in waveform between absorbance and PA intensity (both normalized) as a function of wavelength for all the contrast agents, with a peak at around 680–700 nm for both absorbance and PA intensity, that tapers downwards towards longer wavelengths. This demonstrates a strong correlation between optical absorption spectra and the PA spectra, which validates our data, as shown in Figure 2(B–F). In PA imaging, the PA intensity induced by optical absorption is proportional to light energy deposition, which is the product of the absorption coefficient and the local light fluence. Thus, the small deviations in trend between absorbance and PA intensities can be attributed to light fluence changes caused by slight variations in laser intensity.

In addition, the PA signal for each contrast agent was spectrally unmixed via linear regression. This allows the isolation of the individual contribution of the contrast agent of interest that can be plotted as a function of concentration, which in turn was used to produce a straight line of best fit based on least-squares regression, for each contrast agent. As shown in Figure 3, the line corresponding to ZnPc has the highest gradient, which corresponds to the highest increase in PA signal for an incremental increase in concentration, when compared to the rest. We hereby define this gradient as a form of relative PA quantum yield (φP), a kind of measure of the efficiency of the conversion of light absorption into PA signal. This is analogous to the fluorescence quantum yield (φF), which measures the efficiency of the conversion of light absorption into fluorescence emission. The relative φP of the 5 compounds are computed and listed in Table 1. These are not absolute values, but arbitrary ratios, which reflect the relative PA strength of one compound against that of another. As shown in Table 1, it has also been reported that these photosensitizers have low fluorescence quantum yields (<0.2) but reasonably high singlet oxygen quantum yields (≈ 0.5). This means that although these photosensitizers can offer high PDT efficacy, they exhibit low fluorescence, which may not be adequate for high contrast diagnostic imaging. However, this limitation can be circumvented by using PA imaging, as shown in this work.

Moreover, on testing these compounds for dark toxicity on oral squamous carcinoma cell line (OSCC) for varying concentrations (1 to 100 μM), they exhibited more than 50% cell viability for concentrations up to 100 μM of PpIX and MB, 50 μM of Ce6 and 10 μM of Sq and ZnPc (supplementary information, Fig S1). This vast range of concentrations tested was inclusive of the *in vivo* dose range for PDT for most of them (see SI Table S1) thus making a point that they can be used as PA imaging contrast agents at concentrations that do not induce much toxicity *in vivo*.

Based on the prioritization of the different photosensitizers for MSOT imaging by phantom analysis, we next evaluated ZnPc *in vivo*,

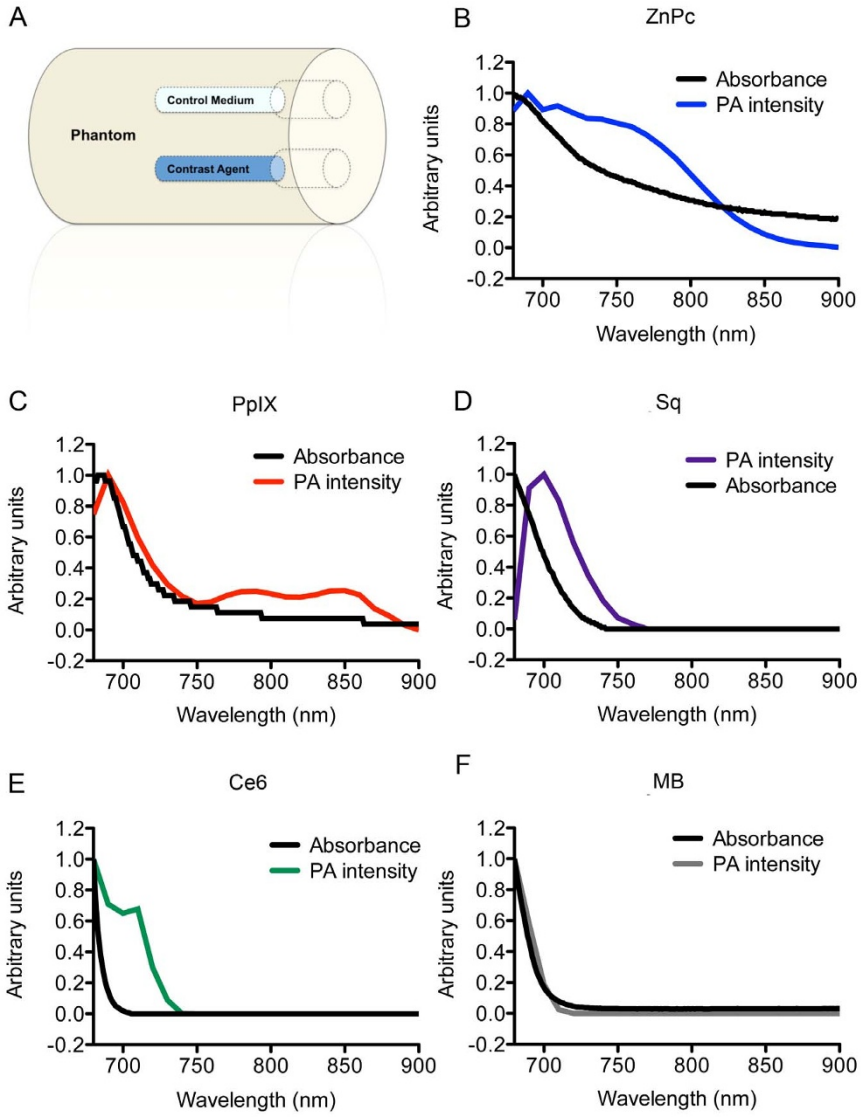

Figure 2 | (A) Phantom schematic. (B–F) Normalized absorbance (black line) and PA intensity (colored line) as a function of wavelength. The strong correlation between optical absorption and the PA effect is illustrated by the similarity in trend between the two graphs for each contrast agent, with a peak at around 680–700 nm, that tapers downwards towards longer wavelengths.

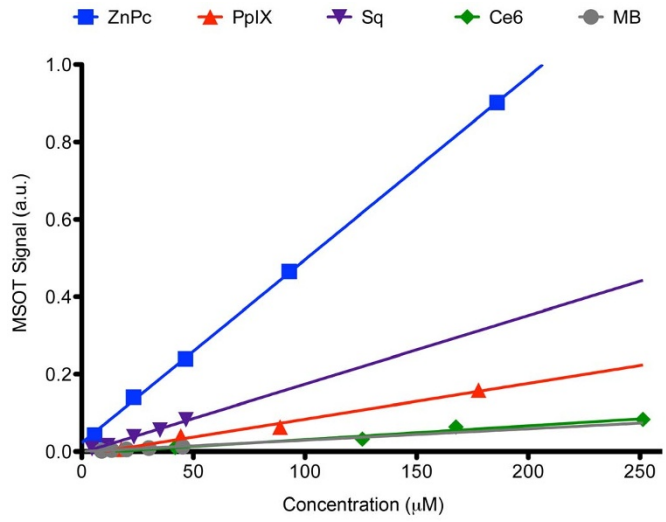

Figure 3 | **Multispectrally unmixed PA signal intensity as a function of concentration with a line of best fit for each contrast agent.**

since it was found to have the strongest PA signal in phantoms. In essence, we injected ZnPc intravenously into mice bearing subcutaneous tumor and monitored the probe uptake over time in the liver, spleen, kidneys, intestines and tumor using PA imaging. We scanned a volume ROI consisting of transverse slices spanning from the liver to the lower abdomen and constructed maximum intensity projections (MIPs) based on these slices for image analysis. A strong *in vivo* MSOT signal of ZnPc was detected in the reticuloendothelial system (liver, spleen), intestines and tumor site within the first hour after injection, with peak accumulation at the 1-hour time point, as shown in the background-corrected images in Figure 4. In addition, the non-background-corrected images in Figure 5 and Figure 6A shows that this signal gradually drops in intensity beyond 1 hour up to a day, suggesting probe clearance within a day. This allows for the rapid evaluation of PDT agent delivery after administration and can aid in optimizing PDT and not full form time point planning. Apart from monitoring the accumulation in tumor, the whole-body biodistribution of compounds can be visualized and quantified simultaneously by MSOT, which can aid in the elucidation of clearance pathways and choosing of optimal dosing strategies. We hypothesize that ZnPc is most likely cleared through the hepatobiliary

Table 1 | Fluorescence, singlet oxygen and relative PA quantum yields of various photosensitizers

Photosensitizers	Fluorescence Quantum Yield (φF)	Singlet Oxygen Quantum Yield (φΔ)	Relative PA Quantum yield (φP)
ZnPc	0.06 [23]	0.62 [23]	0.47
PpIX	0.16 [23]	0.56 [23]	0.093
Sq	0.037 [27]	0.61–0.74 [28]	0.18
Ce6	0.19 [23]	0.65 [23]	0.036
MB	0.02 [23]	0.55 [23]	0.029

system, because high concentrations are found in the liver and intestines up to the 3-hour time point, whereas renal signal is much weaker in comparison, as shown in Figure 5 and Figure 6A. In addition, Figure 6B also shows a peak tumor-to-muscle ratio of the MSOT signal at the 1-hour time point, making this time point ideal for PDT illumination and subsequent monitoring via MSOT imaging. Thus, in summary, the strong MSOT signals from ZnPc observed in the tumor region at the 1-hour time point suggests that MSOT imaging, combined with PDT, offers a novel theranostic approach with high translational potential.

Conclusion

In this work, we demonstrated that various classes of photosensitizers can be used as efficient novel contrast agents for PA imaging. Initially, we carried out the PA study in a phantom model and compared the performance of various classes of photosensitizers. Among the tested compounds, ZnPc was found to be the strongest in terms of PA signal with the highest relative PA quantum yield. Subsequently, we studied the *in vivo* localization and biodistribution of ZnPc in a preclinical animal model of cancer. The preferential accumulation of photosensitizers in tumors is due to the enhanced permeation and retention (EPR) effect that enables us to achieve longitudinal monitoring of cancer. In addition, unlike fluorescence imaging, PA imaging of photosensitizers is free from interference from photobleaching and autofluorescence. Moreover, MSOT imaging allows us to detect endogenous absorbers such as oxygenated and deoxygenated hemoglobin so that tumor blood vasculature and oxygenation status can be monitored at the same time. In addition, it has been reported that many well-studied photosensitizers have low fluorescence quantum yields (<0.2) but reasonably high singlet oxygen quantum yields (≈ 0.5). This means that although these photosensitizers can offer high PDT efficacy, they exhibit low fluorescence, which may not be adequate for high contrast diagnostic imaging. In this study, we have successfully demonstrated that these compounds offer reasonably strong PA signals, which offers a potential alternative imaging technique, on top of fluorescence imaging. In future studies, more work will be devoted towards *in vivo* multifunctional imaging and therapeutic initiatives, such as longitudinal PA monitoring of tumor regression in response to photodynamic therapy for instance, as well as the design of drug carrier systems such as liposomes[29–31] for reduced probe aggregation in blood, as well as enhanced tumor delivery and uptake.

Methods

Preparation of PA contrast agents. Zinc phthalocyanine, protoporphyrin IX, methylene Blue and 2,4-bis [4-(N,N-dibenzylamino)-2,6-dihydroxyphenyl] squaraine in powder form were purchased from Sigma-Aldrich. Chlorin e6 was purchased from Frontier Scientific (Logan, UT). Stock solutions of all compounds were prepared in DMSO. Formulations for absorbance measurements and animal studies were made in 10% DMSO.

UV Absorbance measurement. The wavelength-dependent absorption spectrum of the contrast agents was measured from 680 to 900 nm using a spectrophotometer (DU 730, Beckman Coulter), which in turn was used as an input spectrum to be used for multispectral post-processing of PA signals.

MSOT experimental parameters and protocol. All phantom and *in vivo* mouse imaging experiments were performed using a real-time multispectral optacoustic tomographic (MSOT) imaging system; inVision 128 (iThera Medical GmbH, Neuherberg, Germany).The phantom is made of polyurethane, cylindrical in shape with a diameter of 2 cm, which is specially designed to mimic the shape, size and optical properties of the mouse (iThera Medical GmbH, Neuherberg, Germany). In addition, it has 2 inner cylindrical channels, each with a diameter of 3 mm, one for holding the control medium and the other for holding the dissolved contrast agent in the same medium, as shown in Figure 2A. Optical excitation was provided by an optical parametric oscillator (OPO) with a tunable NIR wavelength range from 680 to 980 nm, which is in turn pumped by a Q-switched Nd:YAG laser with a pulse duration of 10 ns and repetition rate of 10 Hz. Light was delivered by a fiber bundle divided into 10 output arms to illuminate the sample from multiple angles around the imaging plane. PA signals were acquired using a 128-element concave transducer array spanning a circular arc of 270°. This transducer array has a central frequency of 5 MHz, which provided a transverse spatial resolution in the range of 150–200 μm. One transverse image slice was acquired from each laser pulse, resulting in a

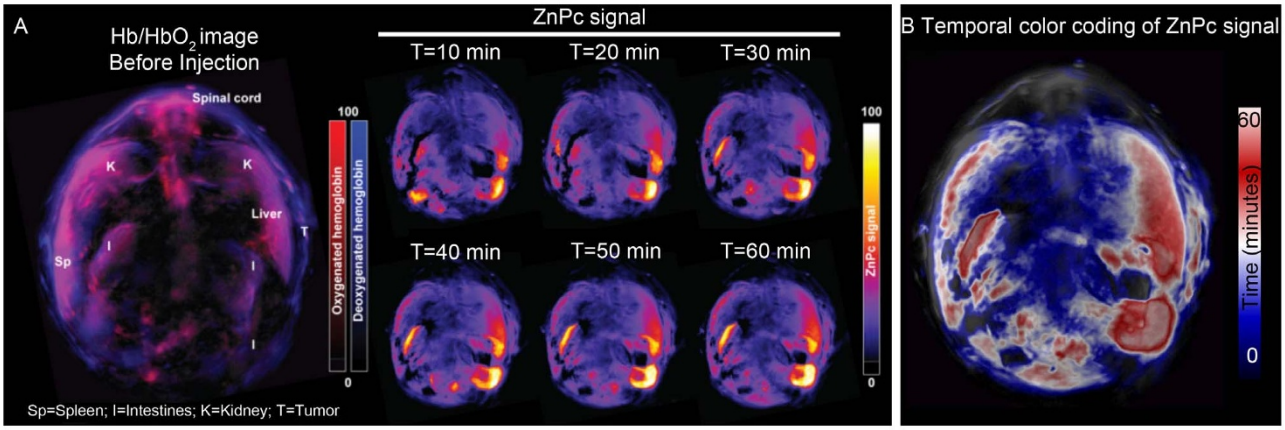

Figure 4 | (A) *In vivo* background-corrected MIP images of transverse slices through mouse preinjection and within the first hour after injection, showing gradual probe accumulation within the tumor site and various organs over time. (B) Time-resolved color coding of the MSOT signal within the first hour after injection, demonstrating peak localization of probe at the tumor site and various organs at 1 hour postinjection. A stack of MIPs of ZnPc signal over time (T = 10–60 mins) is condensed in a parametric map visualizing the T_{max} of ZnPc; peak concentrations of ZnPc are observed at T = 60 mins.

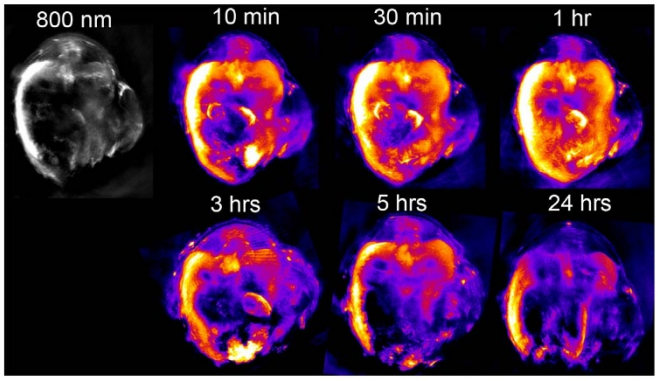

Figure 5 | ***In vivo*** **non-background-corrected MIP images of transverse slices through mouse at various time points postinjection, demonstrating strong probe MSOT signals within the liver, spleen, kidneys, intestines and tumor site.** There is a gradual decrease in the tumor MSOT signal over time, which in turn implies probe clearance within a day.

frame-rate of 10 Hz. During image acquisition, the sample is translated through the transducer array along its axis across the volume ROI, in order to capture the corresponding transverse image slices. For *in vivo* imaging, ultrasound gel was applied on the mouse skin surface and measurements were recorded in a temperature-controlled water for good acoustic coupling. An animal holder with a thin polyethylene membrane was used to prevent direct contact between the mouse and the water.

Animal preparation. All animal experimental procedures were performed in accordance with the protocol #120774 approved by the Institutional Animal Care and Use Committee (IACUC). Xenograft mice models were established by injecting subcutaneously into the right flank of mouse, 0.2 mL of cell suspension containing 5–6 $\times$ 10^6 MCF-7, a human metastatic breast cancer cell line or OSCC, a human oral squamous carcinoma cell line and matrigel (BD biosciences) in 1 : 1 volume ratio. When the tumor volume reached a palpable size, the mouse was used for *in vivo* PA imaging.

In vivo longitudinal monitoring of probe biodistribution in mouse xenograft model. ZnPc at a dosage of 0.21 mg/kg was injected via a catheter into the tail vein of tumor-bearing mice anaesthetized under isoflurane and the probe biodistribution was monitored over time in various organs using PA imaging. Before image acquisition, a volume ROI consisting of transverse slices with a step size of 0.3 mm spanning from the liver to the lower abdomen was selected by manual inspection of live MSOT images, and the 6 laser excitation wavelengths of 680, 700, 750, 800, 850 and 900 nm were selected for correspondence with the major turning points in the absorption spectra of ZnPc, oxy- and deoxy-haemoglobin. Multispectral imaging was then performed with 10 signal averages per wavelength per transverse slice, before injection, during injection and 1, 3, 5, and 24 hr postinjection.

Image reconstruction and multispectral processing. Images were reconstructed using a model-based approach[32] for offline analysis. After image reconstruction, spectral unmixing was performed to resolve individual components from different chromophores in the system. For each pixel in the image, the method fits the total measured optoacoustic spectrum to the known absorption spectra of the individual chromophores, based on least-squares linear regression.

Image processing. Maximum intensity projection (MIP) images were prepared and presented in Figure 4 and 5, for better display of anatomy and quantification. For the first hour in Figure 4, the difference between the time-point images and the prescan image (before injection) were displayed, which is possible because the animal is intact and anaesthetized in the MSOT machine within the 1st hour. For the later time points, this background subtraction is not possible, as the animal is removed and placed in the MSOT system repeatedly, with repositioning, in order to avoid overdosage of isoflurane for the entire 24-hour duration. Although Figure 5 is not background-corrected, it still shows the biodistribution trend over the entire duration.

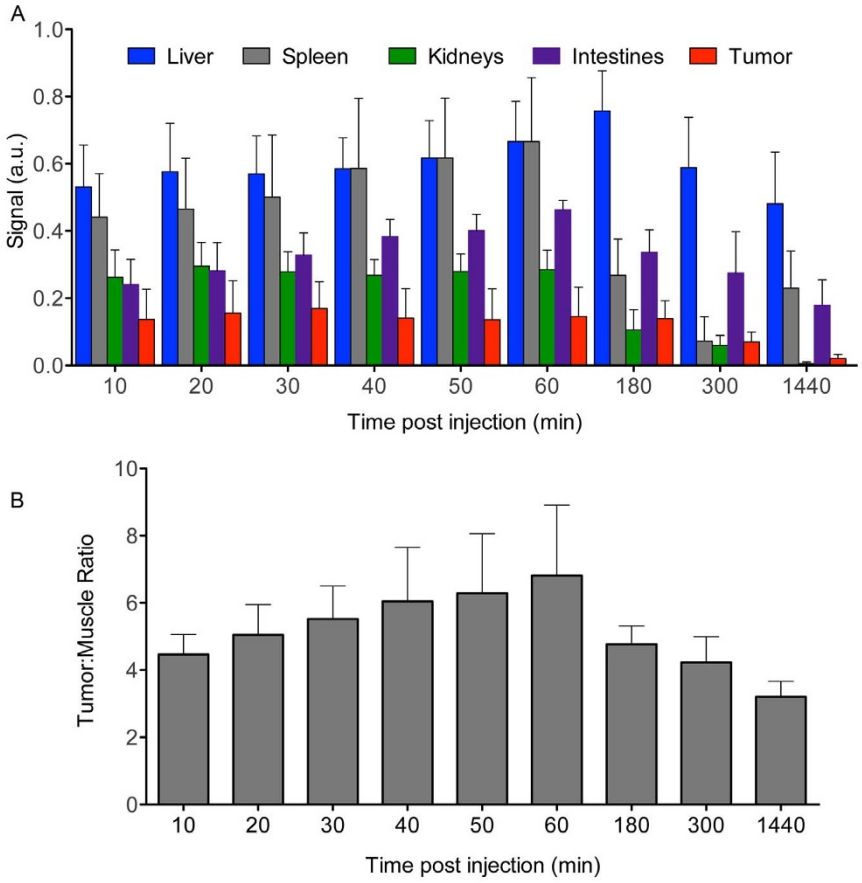

Figure 6 | (A) Biodistribution of ZnPc at various organs and tumor at points. (B) Tumor-to-muscle ratios of MSOT signal at multiple time points (n = 4). Tumor-to-muscle ratio of the MSOT signal peaks at 1-hour, thus making this time point ideal for PDT illumination and subsequent monitoring via MSOT imaging.

1. Wang, L. V. & Hu, S. Photoacoustic tomography: *In vivo* imaging from organelles to organs. *Science* **335**, 1458–1462 (2012).
2. Wang, L. V. Multiscale photoacoustic microscopy and computed tomography. *Nat. Photonics* **3**, 503–509 (2009).
3. Yao, J. & Wang, L. V. Photoacoustic microscopy. *Laser & Photonics Rev.* **7**, 758–778 (2013).
4. Vakoc, B. J., Fukumura, D., Jain, R. K. & Bouma, B. E. Innovation: Cancer imaging by optical coherence tomography: preclinical progress and clinical potential. *Nat. Reviews Cancer* **12**, 363–368 (2012).
5. Ku, G., Wang, X., Xie, X., Stoica, G. & Wang, L. V. Imaging of tumor angiogenesis in rat brains *in vivo* by photoacoustic tomography. *Appl. Opt.* **44**, 770–775 (2005).
6. Stein, E. W., Maslov, K. & Wang, L. V. Noninvasive, *in vivo* imaging of blood-oxygenation dynamics within the mouse brain using photoacoustic microscopy. *J. Biomed. Opt.* **14**, 020502 (2009).
7. Burton, N. C. *et al.* Multispectral optoacoustic tomography (MSOT) of the brain and glioblastoma characterization. *NeuroImage* **65**, 522–528 (2013).
8. Buehler, A., Kacprowicz, M., Taruttis, A. & Ntziachristos, V. Real-time handheld multispectral optoacoustic imaging. *Opt. Lett.* **38**, 1404–1406 (2013).
9. Kruger, R. A., Lam, R. B., Reinecke, D. R., del Rio, S. P. & Doyle, R. P. Photoacoustic angiography of the breast. *Med. Phys.* **37**, 6096 (2012).
10. Luke, G. P., Yeager, D. & Emelianov, S. Y. Biomedical applications of photoacoustic imaging with exogenous contrast agents. *Ann. Biomed. Eng.* **40**, 422–437 (2012).
11. Kircher, M. F. *et al.* A brain tumor molecular imaging strategy using a new triple-modality MRI-photoacoustic-Raman nanoparticle. *Nat. Med.* **18**, 829–834 (2012).
12. de la Zerda, A. *et al.* Family of enhanced photoacoustic imaging agents for high-sensitivity and multiplexing studies in mice. *ACS Nano.* **6**, 4694–4701 (2012).
13. de la Zerda, A. *et al.* Ultrahigh sensitivity carbon nanotube agents for photoacoustic molecular imaging in living mice. *Nano Lett.* **10**, 2168–2172 (2010).
14. de la Zerda, A. *et al.* Carbon nanotubes as photoacoustic molecular imaging agents in living mice. *Nat. Nanotech.* **3**, 557–562 (2008).
15. Buehler, A. *et al.* High resolution tumor targeting in living mice by means of multispectral optoacoustic tomography. *EJNIMMI Research.* **2** (2012).
16. Taruttis, A., Morscher, S., Burton, N. C., Razansky, D. & Ntziachristos, V. Fast multispectral optoacoustic tomography (MSOT) for dynamic imaging of pharmacokinetics and biodistribution in multiple organs. *PLoS ONE* **7**, e30491 (2012).
17. Herzog, E. *et al.* Optical imaging of cancer heterogeneity with multispectral optoacoustic tomography. *Radiology.* **263**, 461–468 (2012).
18. Taruttis, A., Herzog, E., Razansky, D. & Ntziachristos, V. Real-time imaging of cardiovascular dynamics and circulating gold nanorods with multispectral optoacoustic tomography. *Opt. Express.* **18**, 19592–19602 (2010).
19. Yang, H.-W. *et al.* Magnetic gold-nanorod/PNIPAAmMA nanoparticles for dual magnetic resonance and photoacoustic imaging and targeted photothermal therapy. *Biomaterials* **34**, 5651–5660 (2013).
20. Rouleau, L. *et al.* VCAM-1-targeting gold nanoshell probe for photoacoustic imaging of atherosclerotic plaque in mice. *Contrast Media Mol. Imag.* **8**, 27–39 (2013).
21. Nie, L. *et al.* In vivo volumetric photoacoustic molecular angiography and therapeutic monitoring with targeted plasmonic nanostars. *Small* (2013). DOI: 10.1002/smll.201302924.
22. Niidome, T. *et al.* PEG-modified gold nanorods with a stealth character for *in vivo* applications. *J. Control. Release.* **114**(3), 343–347 (2006).
23. Lovell, J. F., Liu, T. W. B., Chen, J. & Zheng, G. Activatable photosensitizers for imaging and therapy. *Chem. Rev.* **110**, 2839–2857 (2010).
24. O'Connor, A. E., Gallagher,W. M. & Byrne, A. T. Porphyrin and nonporphyrin photosensitizers in oncology: preclinical and clinical advances in photodynamic therapy. *Photochem. Photobiol.* **85**, 1053–1074 (2009).
25. Abuteen, A. *et al.* The evaluation of NIR-absorbing porphyrin derivatives as contrast agents in photoacoustic imaging. *Phys. Chem. Chem. Phys.* (2013). DOI: 10.1039/C3CP52193A.
26. Greish, K. Enhanced permeability and retention (EPR) effect for anticancer nanomedicine drug targeting. *Cancer Nanotech. Methods Mol. Biol.* **624**, 25–37 (2010).
27. Kamat, P. V. *et al.* Excited-state properties and photosensitization behaviour of bis(2,4-dihydroxyphenyl)squaraine. *J. Chem. Soc., Faraday Trans.* **89**, 2397–2402 (1993).
28. Yano, S. *et al.* Current states and future views in photodynamic therapy. *J. Photochem. Photobiol. C: Photochem. Rev.* **12**, 46–67 (2011).
29. van Leengoed, H. L. L. M. *et al.* In vivo fluorescence and photodynamic activity of zinc phthalocyanine administered in liposomes. *Br. J. Cancer.* **69**, 840–845 (1994).
30. Isele, U., Schieweck, K., Kessler, R., van Hoogevest, P. & Capraro, H.-G. Pharmacokinetics and body distribution of liposomal zinc phthalocyanine in tumor-bearing mice: influence of aggregation state, particle size, and composition. *J. Pharm. Sci.* **84**, 166–173 (1995).
31. Inés, Y. E. *et al.* Biodistribution of photothera peutic properties of zinc (II) 2, 9, 16, 23-tetrakis (methooxy) phthalocyanine in vivo. *Photodiagn. Photodyn. Therapy.* **6**, 62–70 (2009).
32. Rosenthal, A., Razansky, D. & Ntziachristos, V. Fast semi-analytical model-based acoustic inversion for quantitative optoacoustic tomography. *IEEE Trans. Med. Imag.* **29**, 1275–1285 (2010).

Acknowledgments

This work is supported by Singapore Bioimaging Consortium, Agency for Science, Technology, and Research, Singapore.

Author contributions

C.J.H.H. and G.B.contributed equally to the work in writing the main manuscript text, performing experiments and preparing figures 1–3. W.D. performed image post-processing and prepared figures 4–6. R.M. helped to perform phantom experiments. C.L.W., U.S.D. and A.B.E.A. helped to perform *in vivo* experiments. V. N. and M.O. oversaw and managed the research project and directions. All authors reviewed the manuscript.

Additional information

Supplementary information accompanies this paper at http://www.nature.com/scientificreports

Competing financial interests: The authors declare no competing financial interests.

How to cite this article: Ho, C.J.H. *et al.* Multifunctional Photosensitizer-Based Contrast Agents for Photoacoustic Imaging. *Sci. Rep.* **4**, 5342; DOI:10.1038/srep05342 (2014).

This work is licensed under a Creative Commons Attribution-NonCommercial-NoDerivs 4.0 International License. The images or other third party material in this article are included in the article's Creative Commons license, unless indicated otherwise in the credit line; if the material is not included under the Creative Commons license, users will need to obtain permission from the license holder in order to reproduce the material. To view a copy of this license, visit http://creativecommons.org/licenses/by-nc-nd/4.0/